Desalination and Water Treatment
www.deswater.com
doi: 10.5004/dwt.2023.30056

313 (2023) 37–48
November

Superhydrophilic MXene/mixed-dimensional clay/polyvinyl alcohol film for solar interfacial evaporation

Wenxiao Mu, Chenxiu Gao, Nan Wang, Yuxuan Liu, Hanxue Sun, Zhaoqi Zhu, Jiyan Li, Weidong Liang*

Department of Chemical Engineering, College of Petrochemical Engineering, Lanzhou University of Technology, Lanzhou 730050, China, Tel.: +86-931-7823125; emails: wdliangh@lut.edu.cn (W. Liang), 799509793@qq.com (C. Gao), 1113455344@qq.com (N. Wang), 574875291@qq.com (Y. Liu), sunhx@lut.edu.cn (H. Sun), zhuzhaoqi@lut.edu.cn (Z. Zhu), lijiyan@lut.edu.cn (J. Li)

Received 13 July 2023; Accepted 14 October 2023

ABSTRACT

For the practical application of green and sustainable Solar Steam Generation Technology, improving solar energy conversion efficiency and salt resistance is particularly important. In this study, the MXene/mixed-dimensional clay/polyvinyl alcohol (MXene/MD-clay/PVA) film was prepared by "salt-assisted" freeze-drying method using (3-aminopropyl)triethoxysilane (KH550) modified mixed-dimensional clay (MD-clay) as the raw material, self-assembled MD-clay and MXene material, and polyvinyl alcohol (PVA) as base film. The film can effectively convert light energy into heat energy under solar irradiation, and has excellent properties such as high photothermal conversion efficiency, super hydrophilicity, and low thermal conductivity. The MXene/MD-clay/PVA film has a low thermal conductivity (0.24056 $W \cdot m^{-1} \cdot K^{-1}$); a strain at break of 7.8% at a tensile strength of 0.7 kPa; a light absorption of about 91%; and a complete infiltration of water droplets on the surface of the rGO/MD-clay/PVA film in only 0.133 s. The prepared MXene/MD-clay/PVA can be used in a wide range of applications at 1 $kW \cdot m^{-2}$. The evaporation rate of the prepared MXene/MD-clay/PVA evaporator was 1.6026 $kg \cdot m^{-2} \cdot h^{-1}$ at 1 $kW \cdot m^{-2}$, with an energy conversion efficiency of 91.7%. The evaporation rate in a 15% NaCl solution was 1.4904 $kg \cdot m^{-2} \cdot h^{-1}$, while the MXene/MD-clay/PVA evaporator provided good purification performance for the organic dye Methylene blue solution.

Keywords: Mixed-dimensional clay; Superhydrophilic film; Salt-resistant; Solar steam generation

1. Introduction

In recent years, population growth and industrialization have led to the scarcity and pollution of freshwater resources in many areas [1–3]. The use of thin film technology for seawater desalination has been one of the ways in which the pressure on freshwater resources has been alleviated [4,5]. Conventional thin-film technologies generally require high pressure to drive them, and thin-film desalination technologies such as reverse osmosis [6], electro-dialysis [7] and conventional thin-film distillers [8,9] use high levels of power. Solar energy is an environmentally friendly, efficient, and renewable energy that can be used to purify seawater and solve the freshwater crisis [10,11]. In the past few years, scientists have developed the concept of interfacial evaporation, where water is evaporated by heating at the "gas–liquid" interface, greatly improving energy efficiency [12,13].

In recent years, various photothermal materials have been used in photothermal conversion thin film materials, such as carbon-based materials [2,14–16], semiconductors [17,18], polymers [19,20] and gels [21,22], etc. Although the raw material cost of carbon-based materials is low, many carbon-based materials are subjected to carbonization, which is relatively energy intensive and does not

* Corresponding author.

result in energy savings [23,24]. Materials based on semiconductors are often expensive and difficult to produce on a large scale [25]. The preparation of polymers and gels is complex and their disposal and biodegradability still need further improvement to avoid secondary contamination [26,27]. MXene materials are a new type of two-dimensional (2D) material that have been used in various fields such as photothermal composites, sensors, batteries, and medical devices in recent years and Ti_3C_2 is one of the MXene material families that is widely used in photothermal conversion materials [28,29]. The Al layer in titanium aluminium carbide (Ti_3AlC_2) is etched away using hydrofluoric acid (HF) to form a 2D layered Ti_3C_2, which has a similar morphology to graphene, as both being layered [30]. Examples, Li et al. [31] prepared a SiO_2/MXene/HPTFE Janus film by coating highly efficient photothermal conversion material MXene nanosheets and low thermal conductivity SiO_2 on the hydrophilic polytetrafluoroethylene (HPTFE) film through a commercial continuous spraying system, which had water treatment with a photothermal evaporation rate of 1.53 $kg{\cdot}m^{-2}{\cdot}h^{-1}$, achieving a uniform and effective 85.6% solar thermal conversion efficiency.

Although MXene materials have excellent photothermal conversion properties, MXene materials have many complex functional groups on their surface (–O, –OH, –F, etc.) and are susceptible to oxidative denaturation [32,33]. Mixed-dimensional (MD) natural clays consist of Pal rods, Mt flakes, and mica, which are produced in Gansu, and are difficult and uneconomical to isolate on a large scale [34]. The interaction between the mixed-dimensional clay modified by a silane coupling agent and MXene material not only prevented the oxidative denaturation of MXene material, but also the addition of MXene material greatly improved the photothermal conversion performance of the prepared composite film [35]. In this chapter, MXene/mixed-dimensional clay/polyvinyl alcohol (MXene/MD-clay/PVA) film was prepared by self-assembling the modified MD-clay and MXene into a 5% polyvinyl alcohol (PVA) solution using (3-aminopropyl)triethoxysilane (KH550) modified MD-clay as raw material.

2. Experimental set-up

2.1. Materials

MD-clay from non-metallic mines of Gansu Linze of China. Sodium hexametaphosphate ($(NaPO_3)_6$) was purchased from Tianjin Guangfu Fine Chemical Research Institute (Tianjin, China). Hydrochloric acid (HCl) was purchased from Tianjin Basifu Co., Ltd., China. Ti_3AlC_2 was purchased from Beike 2D Materials Co., Ltd., (China). (3-aminopropyl) triethoxysilane (KH550) was purchased from Shandong Xiya Chemical Co., China. PVA was purchased from Aladdin Chemical Reagent Co., Ltd., China. Glutaraldehyde (50%) was supplied from Shanghai Zhongqin Chemical Reagent Co., Ltd., (China). All other chemical reagents were of analytical grade and do not require further purification.

2.2. Pretreatment of MD-clay

10 g of MD-clay was added to 200 mL of deionized water and stirred at room temperature for 1 h. 0.5 g of sodium hexametaphosphate ($(NaPO_3)_6$) was then added and stirred for a further 12 h. After standing overnight, the sediment at the bottom was removed. The upper suspension was taken, 5 mL of HCl was added to the suspension (to further remove impurities and increase the specific surface area) and stirring was continued at room temperature for 12 h. The solvent was then removed by centrifugation and washed with deionized water to pH = 7. The resulting solid was dried at 75°C. The solid obtained was crushed in a mortar and then passed through a 200-mesh sieve to obtain the acidified MD-clay.

2.3. Preparation of Ti_3C_2

2.5 mL of deionized water and 7.5 mL of HCl were measured and mixed well in a centrifuge tube and placed on a thermostatic magnetic stirrer for stirring. Then, 0.5 g of lithium fluoride was added and slowly added to the centrifuge tube and the temperature of the thermostat stirrer was adjusted to 41°C. Transferred 0.5 g of Ti_3AlC_2 slowly in batches into a centrifuge tube (taking care not to spill it on the wall), then sealed the tube with cling film and punched a few holes in the cling film and react for 48 h. At the end of the reaction, centrifuged at 10,000 rpm for 5 min each time and kept washing by centrifugation with deionized water until the supernatant had pH = 7. After washing, the solid product was mixed with deionized water and sonicated for 1 h in an ice bath to exfoliate the multi-layered MXene into fewer or single-layered nanosheets. The sonicated MXene solution was centrifuged at 3,500 rpm for 8 min and the upper layer was freeze-dried to give the final Ti_3C_2 powder.

2.4. Preparation of MXene/MD-clay/PVA film

0.128 g Ti_3C_2 powder and 0.128 g MD-clay were added to a 100 mL beaker with 40 mL deionized water and stirred in a magnetic stirrer. 0.112 g APS and 100 μL KH550 were added slowly to the beaker, respectively and stirred at room temperature for 4 h. After the reaction, the solid powder was washed continuously by centrifugation with deionized water until the pH = 7 of the supernatant, centrifuged at 3,500 rpm for 5 min and then dried.

2 g of PVA and 50 mL of deionized water were added to a round bottom flask and transferred to an oil bath, condensed and refluxed with constant stirring. The solid powder was transferred to a round bottom flask and the reaction was carried out at 90°C for 2 h. At the end of the reaction, a viscous colloidal film casting solution was obtained.

The film was prepared using a "salt-assisted" process, where the film casting solution was uniformly dripped onto the salt flakes and then freeze-dried. The prepared films were cross-linked with 2.5% glutaraldehyde steam for 2 h, then placed in water to remove the salt and dried at room temperature. The final film was named MXene/MD-clay/PVA film.

A comparative experimental sample without MD-clay was prepared in the same way and named MXene/polyvinyl alcohol (MXene/PVA) film.

3. Results and discussion

The process of preparing MXene/MD-clay/PVA film is shown in Fig. 1. MD-clay was firstly used to remove

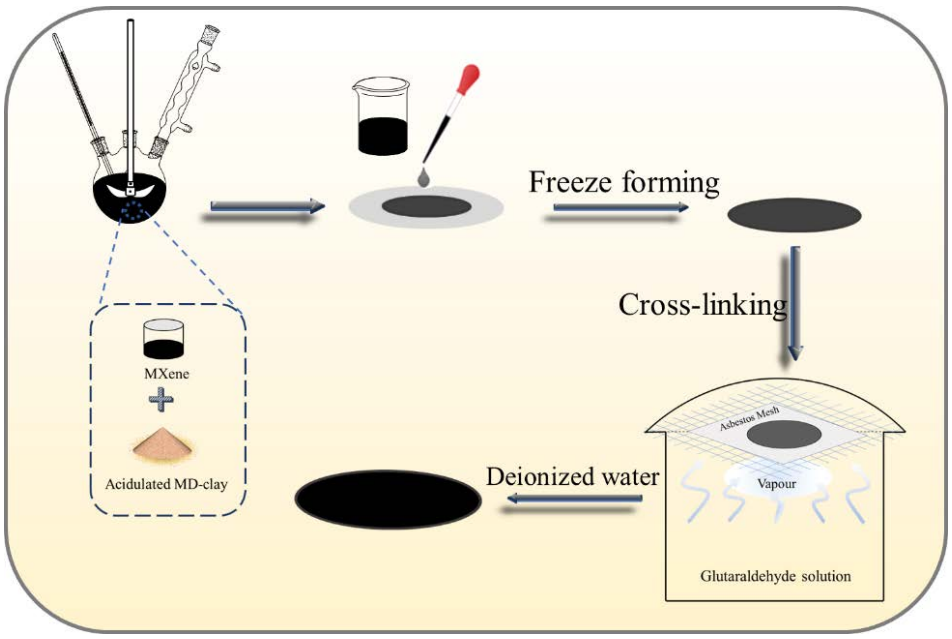

Fig. 1. Schematic diagram of the MXene/MD-clay/PVA film preparation process.

impurities with acid treatment resting method and MXene material was etched by hydrofluoric acid to remove the Al layer from Ti_3AlC_2. Then a single layer of 2D Ti_3C_2 nanosheets was prepared by ultrasonic peeling method. The mixed-dimensional clay and Ti_3C_2 nanosheets were modified by KH550 to have good compatibility, and then the complex was added to the PVA solution to form a well-mixed cast film solution. After defoaming by standing, the cast film solution was uniformly dropped onto the salt flakes and then freeze-dried. The dried film is cross-linked in glutaraldehyde vapor. To remove excess salt, the film was soaked in deionized water and dried at room temperature to prepare MXene/MD-clay/PVA film. the film obtained with the addition of MXene material, exhibits a black surface for absorbing more sunlight for interfacial evaporation of solar energy, which makes it a good candidate.

3.1. Conformational characterisation of MXene materials and MXene/MD-clay/PVA film

The microscopic morphology of the MXene material, MXene/PVA film and MXene/MD-clay/PVA film were characterised by scanning electron microscopy. Fig. 2a and b show a comparison of the morphology of the MXene material, Ti_3C_2 nanosheets, before and after etching, respectively. As shown in Fig. 2a, before etching Ti_3AlC_2 was a stacked multilayer structure with fine gaps between layers. When the Al layer was etched off by adding HF acid and ultrasonically exfoliated, a Ti_3C_2 nanosheet with few or single layers was formed, as shown in Fig. 2a. The microscopic morphology shows that the surface of the prepared Ti_3C_2 nanosheets is smooth and free from other impurities, indicating that the product has been successfully etched and of high purity. The morphology of the MXene/PVA film and MXene/MD-clay/PVA film prepared by the freeze-drying method is shown in Fig. 2c–f. Fig. 2c and f at different magnifications show that the MXene material and PVA composite freeze-dried formed a multi-hollow network-like structure with variable pore size, which was difficult to regulate and had severe agglomeration. As shown in Fig. 2D and e when mixed-dimensional clay is added to the MXene/PVA film system, the prepared film has a larger pore structure, and the mixed-dimensional clay and MXene material are connected in chains by PVA macromolecular chains, forming an intricate chain-like structure. The formation of this chain-like structure facilitates the escape of water molecules in solar interfacial evaporation. As Fig. 2g–i represent the energy-dispersive X-ray spectroscopy image of the MXene/MD-clay/PVA film, it can be seen that the elements C, Si, and Ti are uniformly distributed on the surface of the MXene/MD-clay/PVA film.

3.2. Chemical structure of MXene/MD-clay/PVA film

The crystal structures of MXene material and MXene/PVA film and MXene/MD-clay/PVA film before and after etching were characterised using X-ray diffraction (XRD). As shown in Fig. 3a, the $2\theta = 9.5°$, 19.2°, 39.0° and 41.8° diffraction peaks correspond to the (002), (004), (104) and (105) crystalline peaks of Ti_3AlC_2, which show that the raw material Ti_3AlC_2 powder used is characterised by high purity and good crystallinity [28]. After the raw Ti_3AlC_2 powder was etched by HF for a long time, the Al layer was etched cleanly and the characteristic diffraction peaks of Ti_3AlC_2 basically disappeared, replaced by the characteristic peaks of typical MXene material at $2\theta = 5.92°$, indicating that 2D Ti_3C_2 nanosheets were synthesized. As shown in Fig. 3b, in the MXene/PVA film, a typical PVA diffraction peak appeared at $2\theta = 20°$, while no diffraction peak of MXene material was detected. The main reason for this is that the intensity of the diffraction peak of MXene material was weaker after the two materials were compounded, and thus did not show up in the XRD pattern. However, when the mixed-dimensional

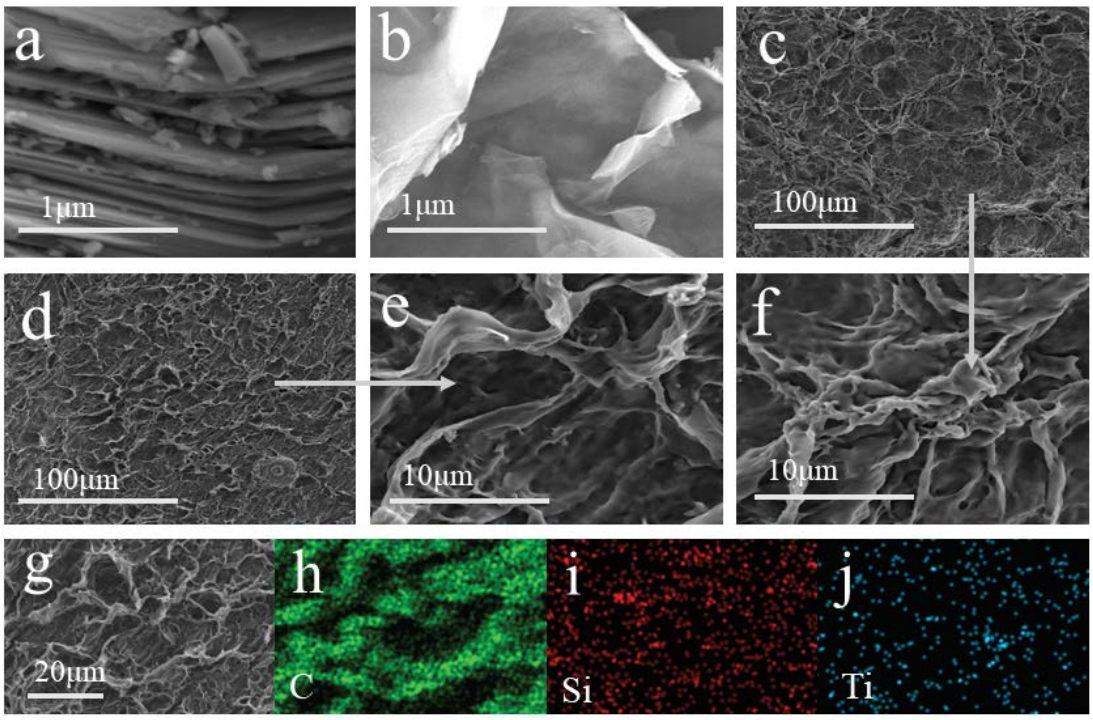

Fig. 2. Scanning electron microscopy images of (a) Ti_3AlC_2, (b) Ti_3C_2 nanosheets, (c,f) MXene/PVA film, (d,e) MXene/MD-clay/PVA film. Energy-dispersive X-ray spectroscopy images of (g–j) MXene/MD-clay/PVA film.

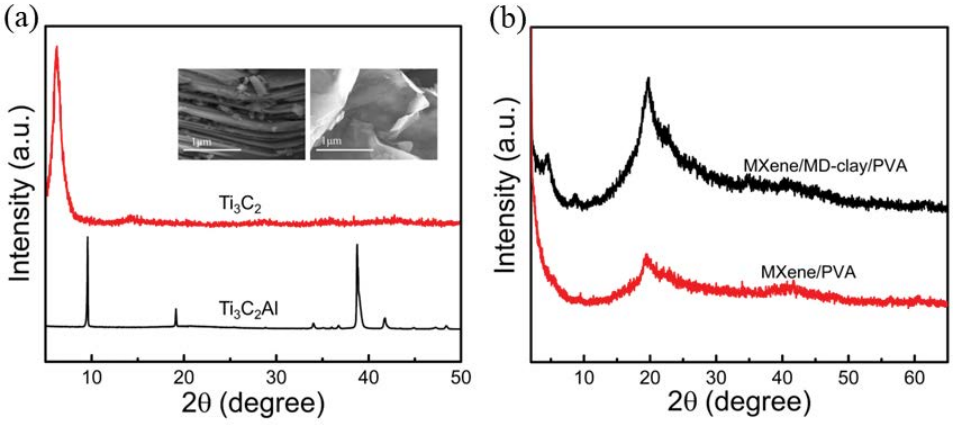

Fig. 3. X-ray diffraction patterns of (a) Ti_3AlC_2 nanosheets and etched Ti_3C_2 nanosheets and (b) MXene/PVA film and MXene/MD-clay/PVA film.

clay was added to the MXene/PVA film, the characteristic diffraction peaks of the mixed-dimensional clay appeared at 2θ = 5.8°, 9.2° and 21.1°, indicating that the mixed-dimensional clay was fully combined with the MXene/PVA film [36].

3.3. MXene/MD-clay/PVA film thermal conductivity and tensile properties

Thermal conductivity is an important indicator to evaluate whether an evaporator is insulated or not. The thermal conductivity of the prepared films was determined by measuring the thermal conductivity of MXene/PVA films, MXene/MD-clay/PVA films and pure water in the wet state. MXene material is a typical thermally conductive material, but when MXene material is laminated with PVA, its thermal conductivity decreases rapidly. When the MXene/PVA film is added to a mixed-dimensional clay with good thermal insulation properties, its thermal conductivity becomes even lower. As shown in Fig. 4a, the thermal conductivity of MXene/MD-clay/PVA film and MXene/PVA film are 0.24056 and 0.307975 $W \cdot m^{-1} \cdot K^{-1}$, respectively lower than that of pure water (0.59 $W \cdot m^{-1} \cdot K^{-1}$). Therefore, the prepared composite film has good thermal insulation properties, which helps to keep heat on the surface of the film, greatly

reducing heat loss and making it a good thermal insulation material.

The mechanical properties of the prepared material are an important factor in assessing the suitability of the film in various environments. The tensile properties of the prepared MXene/PVA film and MXene/MD-clay/PVA film in the wetted condition were compared by a universal testing machine. As shown in Fig. 4b, the strain at break was 7.5% for MXene/PVA film at a pressure of 0.6 kPa and 7.8% for MXene/MD-clay/PVA film at a pressure of 0.7 kPa. At a strain of around 6%, inflection occurs in the tensile curves of both MXene/PVA film and MXene/MD-clay/PVA film, which may be caused by the elasticity of the prepared film in its wet state. The experimental results show that when mixed-dimensional clay is added to the MXene/PVA film, the mixed-dimensional clay will interact with the MXene material and PVA to form hydrogen bonds to enhance the mechanical properties of the film.

3.4. MXene/MD-clay/PVA film surface wettability

In addition, a two-dimensional water exchange evaporator is also designed, as shown in Fig. S1. Polypropylene foam (PP) was used as thermal insulation material, and a layer of gauze was wrapped on the surface of PP for two-dimensional water transfer. The gauze is hydrophilic, which is convenient for water transfer and is not easy to break during water evaporation. By keeping the film and the insulating layer wet, the water molecules on the surface of the film and the evaporator are bonded together by intermolecular forces. The hydrophobic properties of the material surface are critical in determining whether water from the lower layer can be delivered to the material surface in a timely manner. The surface wetting properties of the prepared MXene/PVA film and MXene/MD-clay/PVA film were measured using a contact angle tester. As shown in Fig. 5, the water droplets were completely wetted on the surface of the MXene/PVA film after 1.976 s, while it only took 0.133 s for the surface of the MXene/MD-clay/PVA film to be completely wetted, and the MXene/MD-clay/PVA film showed good hydrophilic properties. The hydrophilic properties of the MXene/MD-clay/PVA film are greatly improved when a hydrophilic MD-clay is added to the MXene/PVA film, resulting in a super hydrophilic film.

3.5. MXene/MD-clay/PVA film pore properties

The pore properties of the MXene/MD-clay/PVA film were measured by mercury pressure and data on the porosity and pore size distribution of the MXene/MD-clay/PVA film were obtained. The results showed that the pore volume of the MXene/MD-clay/PVA film was approximately 0.4765 $mL \cdot g^{-1}$ with an average diameter of 180.3 nm. As shown in Fig. 6a, the immersion and extrusion curves of mercury did not match perfectly, indicating that the pore connectivity obtained by freeze-drying was poor. Furthermore, it can be seen from Fig. 6b that the prepared films have the presence of large pores with a wide distribution. The presence of pore channels facilitates the escape of water molecules and the diffusion of salt ions during the interfacial evaporation process.

3.6. MXene/MD-clay/PVA film light absorption properties

The light absorption properties of MXene/PVA film and MXene/MD-clay/PVA film in the wet state were measured using UV-Vis-NIR spectroscopy and the results are shown in Fig. 7. MXene material has a high light absorption capacity, so adding MXene material to the film can effectively improve the light absorption rate. The light absorption rate of MXene/PVA film (about 91%) than the MXene/MD-clay/PVA film (about 82%) due to the brick-red colour of the Linze mixed-dimensional clay, which was added to the MXene/PVA system to produce a film with a dark brown surface. Overall, the two films prepared have high light absorption properties and can effectively convert light energy into heat energy and facilitate the evaporation of water vapour.

3.7. MXene/MD-clay/PVA film interfacial evaporation performance

The interfacial evaporation performance of the prepared films under simulated indoor lighting was measured

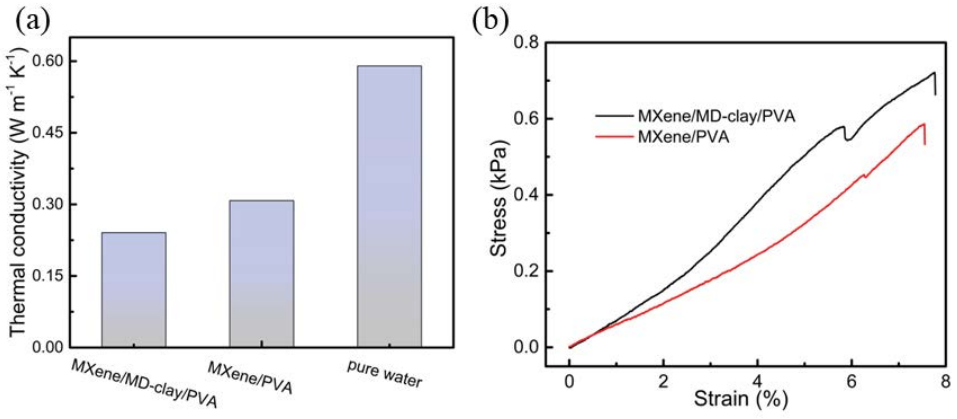

Fig. 4. (a) Thermal conductivity of MXene/PVA film, MXene/MD-clay/PVA film and pure water in the wetted condition. (b) The tensile curves of MXene/PVA film and MXene/MD-clay/PVA film in the wetted condition.

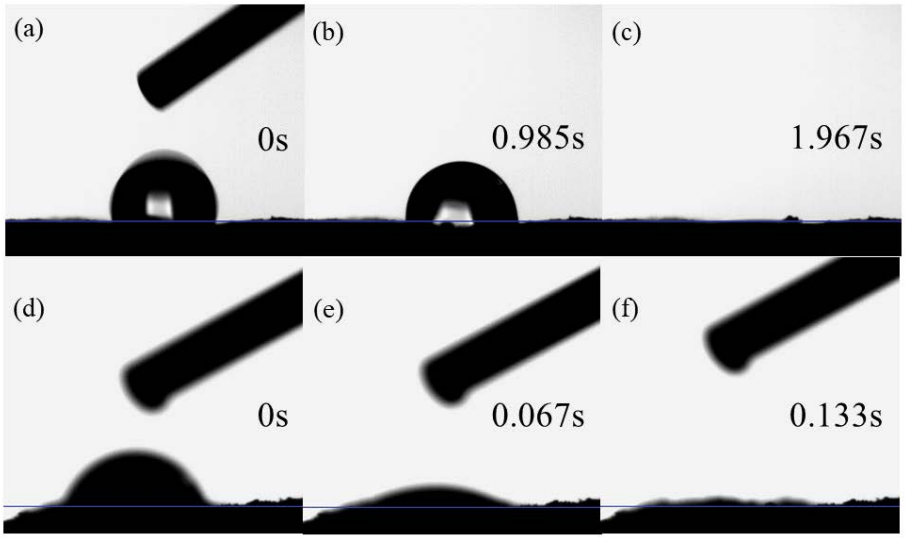

Fig. 5. Variation of water contact angle of (a) MXene/PVA film in 1.967 s and (b–f) MXene/MD-clay/PVA film in 0.133 s.

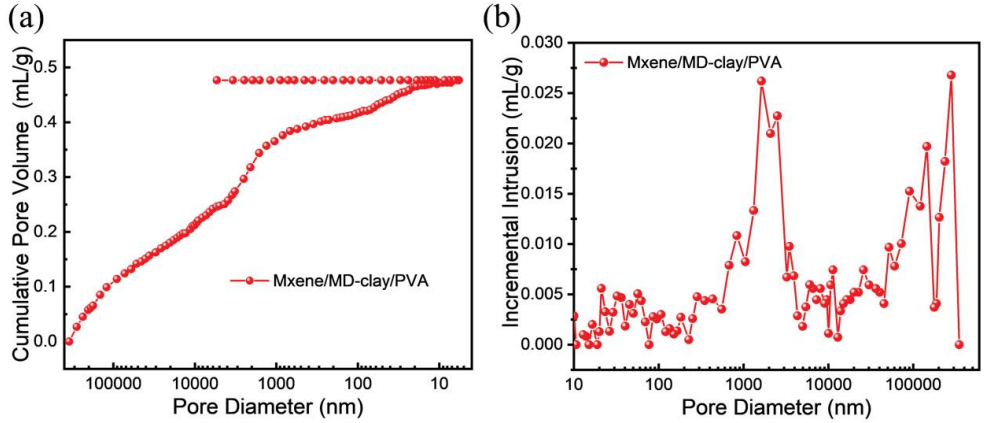

Fig. 6. (a) Mercury intrusion/extrusion curves of MXene/MD-clay/PVA film and (b) pore-size distribution of MXene/MD-clay/PVA film.

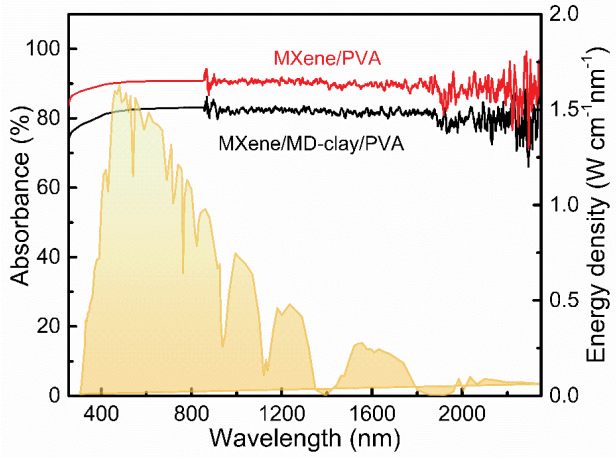

Fig. 7. Light absorption curves of MXene/PVA film and MXene/MD-clay/PVA film.

on a home-made solar interfacial evaporation system in the laboratory, as shown in Fig. 8. The performance of the evaporators was assessed by comparing the evaporated mass of water with time for pure water (no evaporator), MXene/PVA evaporator and MXene/MD-clay/PVA evaporator at 1 kW·m^{-2}. As shown in Fig. 8a, the water evaporation masses for the pure water, MXene/PVA evaporator and MXene/MD-clay/PVA evaporator were 0.7062, 1.5402 and 1.6026 kg·m^{-2}, respectively, within 1 h. From the graph it can be seen that in the same time the MXene/MD-clay/PVA evaporator is higher than the water evaporation of pure water and MXene/PVA evaporator, which shows that the prepared MXene/MD-clay/PVA evaporator has the best performance. As shown in Fig. 8b, the evaporation rates and evaporation efficiencies were calculated to be 0.7062 kg·m^{-2}·h^{-1}, 1.5402 kg·m^{-2}·h^{-1}, 1.6026 kg·m^{-2}·h^{-1} and 40.3%, 87.4% and 91.7% for the pure water, MXene/PVA evaporator and MXene/MD-clay/PVA evaporator, respectively. The photothermal conversion efficiency of MXene/MD-clay/PVA

evaporator is as high as 91.7%. The value is much higher than that of previously reported evaporators (Table S1).

To further investigate the stability of the evaporation performance of the MXene/MD-clay/PVA evaporator. 10 cycles of experiments were tested on the same sample for 1 h per cycle and the results are shown in Fig. 8c. The experimental results show that the same sample maintained an energy conversion efficiency of more than 80% in all 10 cycles, indicating that the MXene/MD-clay/PVA evaporator maintained a high evaporation rate and energy conversion efficiency over a long period of operation.

During the evaporation of the water, the temperature changes on the surface of the MXene/MD-clay/PVA evaporator were recorded using an infrared camera and the results are shown in Fig. 8d. Within the first 300 s, the surface temperatures of pure water, MXene/PVA evaporator and MXene/MD-clay/PVA evaporator increased from 25.9°C, 25.2°C and 25.9°C to 27.5°C, 40.5°C and 39.5°C, respectively. The surface temperatures of MXene/PVA evaporator and MXene/MD-clay/PVA evaporator increased rapidly. The surface temperatures of the MXene/PVA evaporator and MXene/MD-clay/PVA evaporator were much higher than the surface temperature of pure water (without evaporator), however, the surface temperature of the MXene/PVA evaporator was slightly higher than the surface temperature of the MXene/MD-clay/PVA evaporator. This is probably mainly due to the lighter color of the MXene/MD-clay/PVA film surface after the addition of the brick-red mixed-dimensional clay. During the period from 300 to 3,600 s, the surface temperature of the MXene/MD-clay/PVA evaporator was maintained at about 41°C. The high surface temperature maintained the rapid evaporation of water molecules on the surface of the MXene/MD-clay/PVA film, thus increasing the evaporation rate of the evaporator. The above results show that the prepared MXene/MD-clay/PVA film has excellent interfacial evaporation performance, which is due to the fact that in addition to having high light absorption and excellent water transport properties, the addition of mixed-dimensional clay reduces the thermal conductivity of the material, which is conducive to improving its thermal insulation performance.

3.8. MXene/MD-clay/PVA film water purification performance

The water purification performance is an important indicator to study whether the solar evaporator can be used in practice. In the experiments in this chapter, different concentrations of NaCl solution, Methylene blue (MB) solution and simulated seawater were selected to evaluate the water purification capacity of the MXene/MD-clay/PVA evaporator and the results are shown in Fig. 9. As seen in Fig. 9a, the evaporation performance was measured in 0%, 5%, 10% and 15% NaCl solutions for 1 h. A slight decrease in water evaporation was measured during the process from 0% NaCl solution (pure water) to 15% NaCl solution. The evaporation rate and energy conversion efficiency

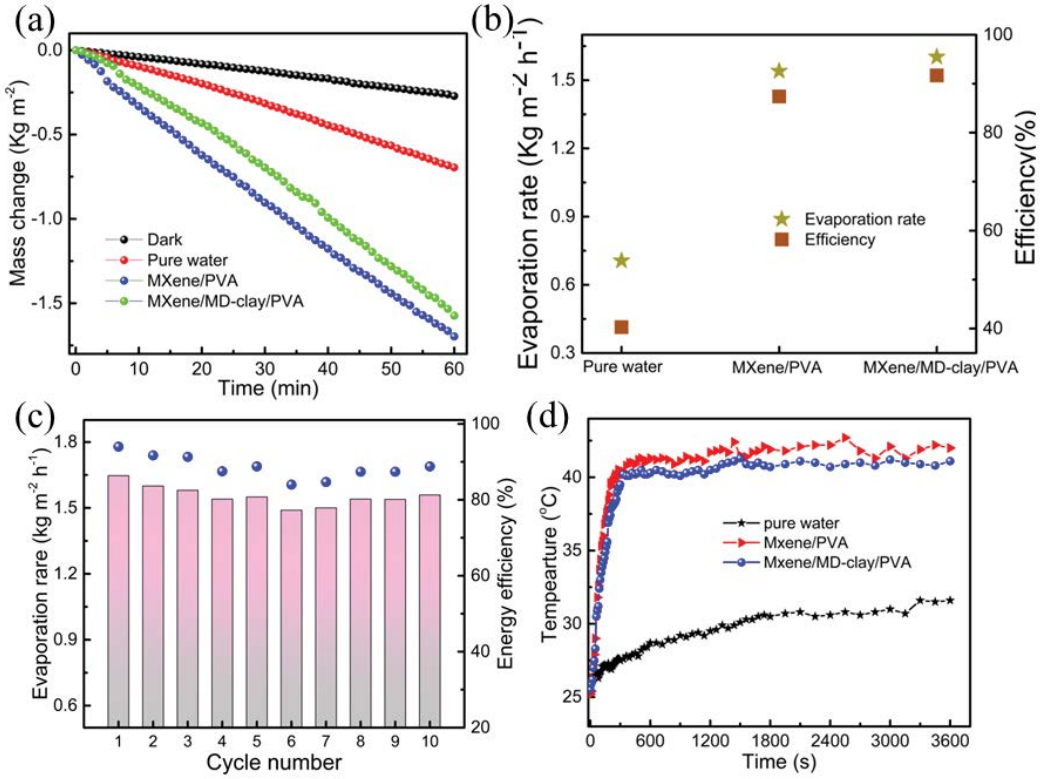

Fig. 8. (a) Water evaporation mass of pure water, MXene/PVA evaporator and MXene/MD-clay/PVA evaporator with time at 1 kW·m^{-2}. (b) Energy conversion efficiency and evaporation rate of pure water, MXene/PVA evaporator and MXene/MD-clay/PVA evaporator. (c) Energy conversion efficiency and evaporation rate of MXene/MD-clay/PVA evaporator in 10 cycles. (d) Surface temperatures of pure water, MXene/PVA evaporator and MXene/MD-clay/PVA evaporator vary with time at 1 kW·m^{-2}.

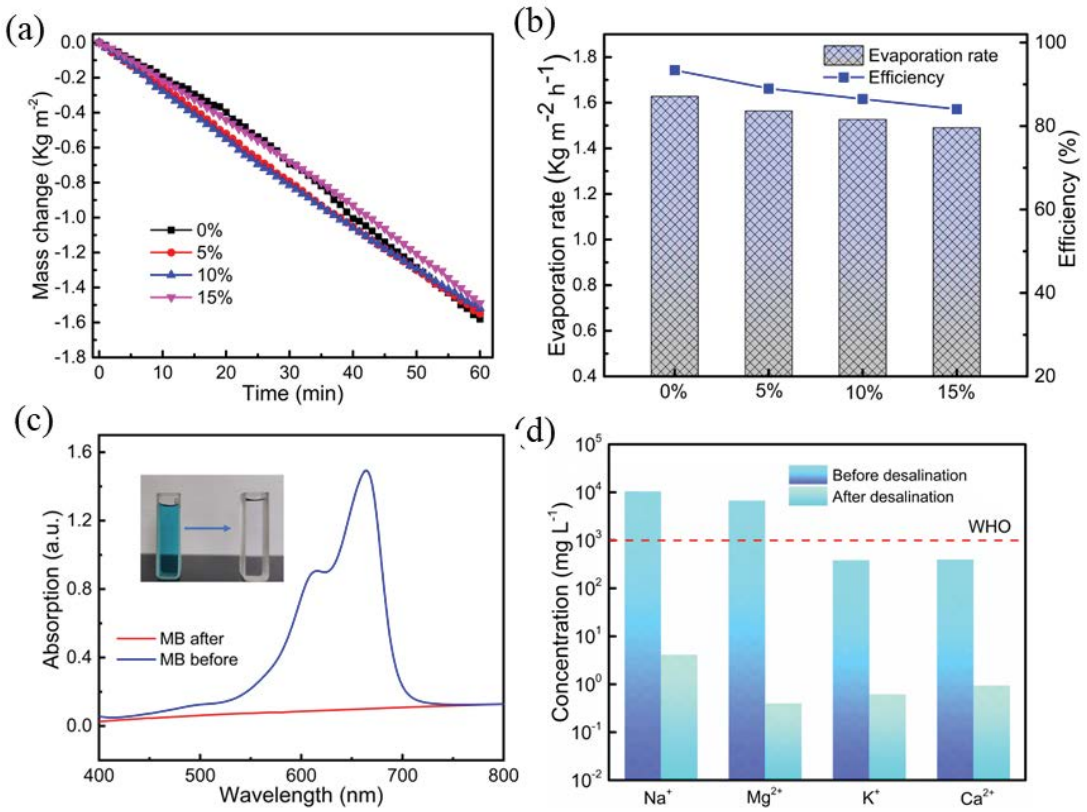

Fig. 9. (a) Mass change of water in the MXene/MD-clay/PVA evaporator in different concentrations of NaCl solution within 1 h. (b) Energy conversion efficiency and evaporation rate of MXene/MD-clay/PVA evaporator in different concentrations of NaCl solution. (c) UV-Vis absorption spectra of Methylene blue solution before and after purification. (d) Changes in the concentration of major ions before and after the purification of MXene/MD-clay/PVA evaporator in simulated seawater.

were calculated for different concentrations of NaCl solutions over 1 h. The evaporation rate decreased from 1.6278 to 1.4904 kg·m^{-2}·h^{-1} and the energy conversion efficiency decreased from 93.6% to 84%. The main reason for the reduction in evaporation and energy conversion efficiency was that the salt ions in the NaCl solution were taken out during the evaporation of water, and the salt ions formed crystals on the evaporator surface, blocking the channels for water molecule transport. The experimental results show that the MXene/MD-clay/PVA evaporator has good salt resistance.

Furthermore, in order to determine the treatment capacity of the MXene/MD-clay/PVA evaporator for organic dye wastewater, the common dye MB was selected for the study, as shown in Fig. 9c. The concentration of the experimentally selected MB solution was calculated from the measured standard curve of the MB solution to be 10.5 mg·L^{-1}. It can be seen in the figure that after purification by the evaporator, the concentration of the MB solution was 0.29 mg·L^{-1} and the MXene/MD-clay/PVA evaporator removed up to 97% of the MB solution. Also, it can be seen in the inset that the colour of the MB solution changed from blue to clear. The results show that the MXene/MD-clay/PVA evaporator is also suitable for the treatment of organic dye wastewater, extending the practical application of the evaporator.

Desalination of seawater is currently the most important way to obtain freshwater resources. The removal capacity of the MXene/MD-clay/PVA evaporator was examined by studying the change in concentration of the main ions in simulated seawater before and after purification. As shown in Fig. 9d, the concentrations of Na^+, Mg^{2+}, K^+ and Ca^{2+} were determined by inductively coupled plasma spectrometry after purification and the concentrations decreased from 10,484; 6,708; 383 and 397 mg·L^{-1}, respectively to 4.118, 0.3998, 0.6187 and 0.9406 mg·L^{-1}, which is much lower than the drinking water standard stipulated by World Health Organization [37]. The above experimental results show that the MXene/MD-clay/PVA evaporator can be efficiently used in high concentration brine, organic dye wastewater and seawater desalination.

4. Conclusions

The MXene/MD-clay/PVA film was prepared by self-assembling the modified hybrid clay and MXene material into 5% PVA solution using KH550 modified MD-clay as raw material. The interaction between the hybrid clay and MXene can effectively prevent the oxidation of Ti_3C_2 nanosheets and improve the photothermal conversion and mechanical properties of the MXene/MD-clay/PVA film. As both the hybrid clay and PVA have hydrophilic properties, the prepared films also exhibit superhydrophilic properties, with water droplets completely infiltrating the film surface within 0.1333 s, providing excellent water transport capabilities. The MXene/MD-clay/PVA film has a low thermal

conductivity (0.2406 $W \cdot m^{-1} \cdot K^{-1}$), a fracture strain of 7.8% at a pressure of 0.7 kPa, and a light absorption of around 91%. The prepared MXene/MD-clay/PVA evaporator showed an evaporation rate of 1.6026 $kg \cdot m^{-2} \cdot h^{-1}$ under 1 $kW \cdot m^{-2}$ simulated light, with an energy conversion efficiency of 91.7%. The energy conversion efficiency remained above 80% in different concentrations of NaCl solution, while the MXene/MD-clay/PVA evaporator also had excellent purification capability for MB solution. The experimental results show that the MXene/MD-clay/PVA evaporator is suitable for dye wastewater treatment and seawater desalination.

Acknowledgements

The authors are grateful to the National Natural Science Foundation of China (Grant No.51962018,52066012), Industrial Support Project of Education Department of Gansu Province (2021CYZC-10), Technology Project of Gansu Province (Grant No. 22CX8GA121).

Credit author statement

Wenxiao Mu: Conceptualization, Methodology, Validation, Formal analysis, Writing-Original Draft, Visualization. Weidong Liang: Conceptualization, Resources, Supervision, Project administration, Funding acquisition, Data Curation, Writing- Reviewing and Editing. Chenxiu Gao: Methodology, Formal analysis. Nan Wang: Formal analysis. Yuxuan Liu: Formal analysis. Hanxue Sun: Formal analysis. Zhaoqi Zhu: Data curation, Resources. Jiyan Li: Methodology, Validation, Formal analysis.

References

[1] F. Dolan, J. Lamontagne, R. Link, M. Hejazi, P. Reed, J. Edmonds, Evaluating the economic impact of water scarcity in a changing world, Nat. Commun., 12 (2021) 1–10.
[2] G. Li, Q. Wang, J. Wang, J. Ye, W. Zhou, J. Xu, S. Zhuo, W. Chen, Y. Liu, Carbon-supported nano tungsten bronze aerogels with synergistically enhanced photothermal conversion performance: fabrication and application in solar evaporation, Carbon N. Y., 195 (2022) 263–271.
[3] M. Cong, F. Wang, Y. Zhang, L. Xie, Y. Lei, K. Sun, L. Dong, An array structure of polydopamine/wood solar interfacial evaporator for high-efficiency water generation and desalination, Sol. Energy Mater. Sol. Cells, 249 (2023) 112052, doi: 10.1016/j.solmat.2022.112052.
[4] A. Politano, P. Argurio, G. Di Profio, V. Sanna, A. Cupolillo, S. Chakraborty, H.A. Arafat, E. Curcio, Photothermal membrane distillation for seawater desalination, Adv. Mater., 29 (2017) 1–6.
[5] J. Yan, Q. Su, W. Xiao, Z. Wu, L. Chen, L. Tang, N. Zheng, J. Gao, H. Xue, A review of nanofiber membranes for solar interface evaporation, Desalination, 531 (2022) 115686, doi: 10.1016/j.desal.2022.115686.
[6] T. Lee, A. Rahardianto, Y. Cohen, Flexible reverse osmosis (FLERO) desalination, Desalination, 452 (2019) 123–131.
[7] G. Doornbusch, M. van der Wal, M. Tedesco, J. Post, K. Nijmeijer, Z. Borneman, Multistage electrodialysis for desalination of natural seawater, Desalination, 505 (2021) 114973, doi: 10.1016/j.desal.2021.114973.
[8] S.S. Ray, S.S. Chen, D. Sangeetha, H.M. Chang, C.N.D. Thanh, Q.H. Le, H.M. Ku, Developments in forward osmosis and membrane distillation for desalination of waters, Environ. Chem. Lett., 16 (2018) 1247–1265.
[9] J. Kim, K. Park, D.R. Yang, S. Hong, A comprehensive review of energy consumption of seawater reverse osmosis desalination plants, Appl. Energy, 254 (2019) 113652, doi: 10.1016/j.apenergy.2019.113652.
[10] C.B. Maia, F.V.M. Silva, V.L.C. Oliveira, L.L. Kazmerski, An overview of the use of solar chimneys for desalination, Sol. Energy, 183 (2019) 83–95.
[11] M. Ginsberg, Z. Zhang, A.A. Atia, M. Venkatraman, D.V. Esposito, V.M. Fthenakis, Integrating solar energy, desalination, and electrolysis, Sol. RRL, 6 (2022) 1–13.
[12] P. Tao, G. Ni, C. Song, W. Shang, J. Wu, J. Zhu, G. Chen, T. Deng, Solar-driven interfacial evaporation, Nat. Energy, 3 (2018) 1031–1041.
[13] M. Jiang, Q. Shen, J. Zhang, S. An, S. Ma, P. Tao, C. Song, B. Fu, J. Wang, T. Deng, W. Shang, Bioinspired temperature regulation in interfacial evaporation, Adv. Funct. Mater., 30 (2020) 1910481, doi: 10.1002/adfm.201910481.
[14] Y. Wu, R. Kong, C. Ma, L. Li, Y. Zheng, Y. Lu, L. Liang, Y. Pang, Q. Wu, Z. Shen, H. Chen, Simulation-guided design of bamboo leaf-derived carbon-based high-efficiency evaporator for solar-driven interface water evaporation, Energy Environ. Mater., 5 (2022) 1323–1331.
[15] H. Sun, Y. Li, J. Li, Z. Zhu, W. Zhang, W. Liang, C. Ma, A. Li, Facile preparation of a carbon-based hybrid film for efficient solar-driven interfacial water evaporation, ACS Appl. Mater. Interfaces, 13 (2021) 33427–33436.
[16] Y. Li, Y. Shi, H. Wang, T. Liu, X. Zheng, S. Gao, J. Lu, Recent advances in carbon-based materials for solar-driven interfacial photothermal conversion water evaporation: assemblies, structures, applications, and prospective, Carbon Energy, (2023) 1–42, doi: 10.1002/cey2.331.
[17] P. Ying, M. Li, F. Yu, Y. Geng, L. Zhang, J. He, Y. Zheng, R. Chen, Band gap engineering in an efficient solar-driven interfacial evaporation system, ACS Appl. Mater. Interfaces, 12 (2020) 32880–32887.
[18] I. Ibrahim, D.H. Seo, A.M. McDonagh, H.K. Shon, L. Tijing, Semiconductor photothermal materials enabling efficient solar steam generation toward desalination and wastewater treatment, Desalination, 500 (2021) 114853, doi: 10.1016/j.desal.2020.114853.
[19] J. Liu, X. Chen, H. Yang, J. Tang, R. Miao, K. Liu, Y. Fang, Gel-emulsion templated polymeric aerogels for solar-driven interfacial evaporation and electricity generation, Mater. Chem. Front., 5 (2021) 1953–1961.
[20] F. Wang, J. Li, W. Bai, C. Wang, A. Li, Recent progress on the solar-driven interfacial evaporation based on natural products and synthetic polymers, Sol. RRL, 5 (2021) 1–22.
[21] L. Chen, Q. Su, Z. Wu, J. Wang, G. Zhang, H. Xue, J. Gao, Fabric interleaved composite hydrogels for high-performance solar-enabled interfacial evaporation, Sci. China Mater., 66 (2023) 2852–2862.
[22] L. Shi, K. Sun, G. Zhang, M. Jiang, X. Xu, X. Zhuang, Hybrid nanofibrous aerogels for all-in-one solar-driven interfacial evaporation, J. Colloid Interface Sci., 624 (2022) 377–384.
[23] Q. Zhang, X. Yang, H. Deng, Y. Zhang, J. Hu, R. Tian, Carbonized sugarcane as interfacial photothermal evaporator for vapor generation, Desalination, 526 (2022) 115544, doi: 10.1016/j.desal.2021.115544.
[24] C. Xu, F. Gao, J. Tang, Y. Yao, T. Liu, Direct laser writing carbonization of polyimide films enabled multilayer structures for the use in interfacial solar-driven water evaporation, J. Mater. Chem. A, 10 (2022) 12692–12701.
[25] Y. Ren, R. Zhou, R. Yang, T.G. Dong, Q. Lu, Systematic review of material and structural design in interfacial solar evaporators for clean water production, Sol. RRL, 7 (2023) 1–25.
[26] L. Qiao, N. Li, L. Luo, J. He, Y. Lin, J. Li, L. Yu, C. Guo, P. Murto, X. Xu, Design of monolithic closed-cell polymer foamsviacontrolled gas-foaming for high-performance solar-driven interfacial evaporation, J. Mater. Chem. A, 9 (2021) 9692–9705.
[27] L. Qiao, S. Li, N. Li, S. Wang, C. Wang, X. Meng, P. Murto, X. Xu, Fabrication of monopile polymer foams via rotating gas foaming: hybrid applications in solar-powered interfacial evaporation and water remediation, Sol. RRL, 6 (2022) 1–13.
[28] M. Malaki, A. Maleki, R.S. Varma, MXenes and ultrasonication, J. Mater. Chem. A, 7 (2019) 10843–10857.

[29] C. Zhou, X. Zhao, Y. Xiong, Y. Tang, X. Ma, Q. Tao, C. Sun, W. Xu, A review of etching methods of MXene and applications of MXene conductive hydrogels, Eur. Polym. J., 167 (2022) 111063, doi: 10.1016/j.eurpolymj.2022.111063.
[30] D. Johnson, Z. Qiao, E. Uwadiunor, A. Djire, Holdups in nitride MXene's development and limitations in advancing the field of MXene, Small, 18 (2022) 2106129, doi: 10.1002/smll.202106129.
[31] H. Li, L. Li, L. Xiong, B. Wang, G. Wang, S. Ma, X. Han, SiO_2/MXene/poly(tetrafluoroethylene)-based Janus membranes as solar absorbers for solar steam generation, ACS Appl. Nano Mater., 4 (2021) 14274–14284.
[32] C. Cai, Y. Wang, Z. Wei, Y. Fu, Biomimetic 3D membranes with MXene heterostructures for superior solar steam generation, water treatment, and electricity generation, Sol. RRL, 5 (2021) 1–12.
[33] X.J. Zha, X. Zhao, J.H. Pu, L.S. Tang, K. Ke, R.Y. Bao, L. Bai, Z.Y. Liu, M.B. Yang, W. Yang, Flexible anti-biofouling MXene/cellulose fibrous membrane for sustainable solar-driven water purification, ACS Appl. Mater. Interfaces, 11 (2019) 36589–36597.
[34] G. Tian, W. Wang, D. Wang, Q. Wang, A. Wang, Novel environment friendly inorganic red pigments based on attapulgite, Powder Technol., 315 (2017) 60–67.
[35] P. Zhou, Q. Zhu, X. Sun, L. Liu, Z. Cai, J. Xu, Recent advances in MXene-based membrane for solar-driven interfacial evaporation desalination, Chem. Eng. J., 464 (2023) 142508, doi: 10.1016/j.cej.2023.142508.
[36] W. Yu, Y. Li, B. Xin, Z. Lu, MXene/PVA fiber-based supercapacitor with stretchability for wearable energy storage, Fibers Polym., 23 (2022) 2994–3001.
[37] Z.C. Xiong, Y.J. Zhu, D.D. Qin, F.F. Chen, R.L. Yang, Flexible fire-resistant photothermal paper comprising ultralong hydroxyapatite nanowires and carbon nanotubes for solar energy-driven water purification, Small, 14 (2018) 1803387, doi: 10.1002/smll.201803387.

Supplementary information

S1. Experimental section

S1.1. Material characterizations

The morphology of the MXene/mixed-dimensional clay/polyvinyl alcohol (MXene/MD-clay/PVA) film was measured by field-emission scanning electron microscopy (MIRA3, TESCAN, Ltd.). The elements and contents in MXene/MD-clay/PVA film was detected by the energy-dispersive X-ray spectrometer (Bruker Nano, Berlin, Germany.). The optical properties of the MXene/MD-clay/PVA film was measured by an ultraviolet-visible-near infrared spectrophotometer equipped with an integrating sphere (Perkin Elmer Lambda 750 S UV/Vis/NIR). The thermal conductivity value of MXene/MD-clay/PVA film was measured by a multi-function rapid thermal conductivity tester (DRE-III, China). The surface wettability of the samples was investigated by the contact angle meter (SZ-CAM, China). The ions concentration of seawater before and after desalination were measured by atomic absorption spectrometer (Jena ContrAA 700, Germany). The sample's surface was illuminated by a solar simulator (Scientech SF300, Canada).

S1.2. Solar steam generation testing

The polypropylene plastic foam was used as the thermal insulation material, which has a thickness of 10 mm. The solar steam generation experiments were conducted at a lab-made, online, a real-time measurement system for 60 min which consisted of (a) a solar light simulator (Xenon Arc Lamp, CEL-S500, Ceaulight), (b) a solar filter (AM 1.5, Ceaulight), (c) an analytical balance with a maximum measuring range of 200 g (FA 2004), (d) a computer to record the real-time mass reduction for steam generation, (e) an infrared camera to record the surface temperature of samples (Testo 869, Germany). Measured light intensity by a full spectrum optical power meter (CEL-NP2000-2A, Beijing China Education Au-light Co., Ltd.).

S1.3. Calculation of the energy conversion efficiency

The solar thermal conversion efficiency (η) was calculated by using the Eq. (1):

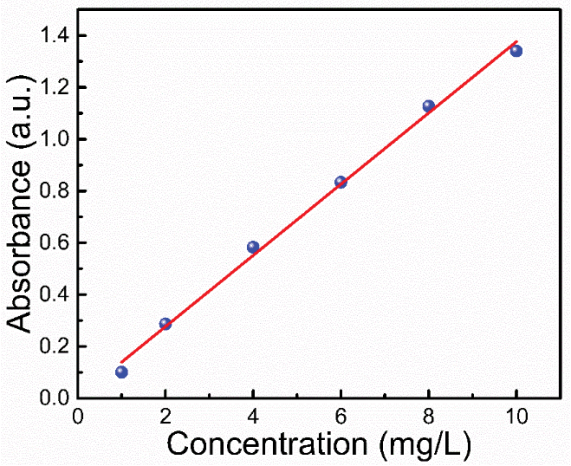

Fig. S2. Standard curve of absorbance of Methylene blue solution and its concentration.

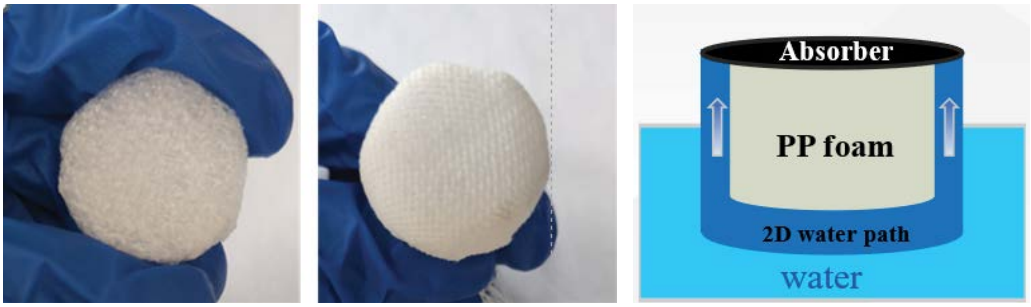

Fig. S1. Digital photographs of the evaporator.

$$\eta = \frac{mh_{Lv}}{C_{opt} \cdot q_i} \quad \text{(S1)}$$

where m is the mass flux of steam (the rate of water evaporation under the dark condition subtracted), C_{opt} is the optical concentration (the number of the sun), q_i is the nominal direct solar irradiation 1 kW·m^{-2} under 1 sun, h_{Lv} denotes total enthalpy of liquid-vapor phase change (including sensible heat ($C\Delta T$) and phase-change enthalpy), can be calculated as:

$$h_{Lv} = \lambda + C\Delta T \quad \text{(S2)}$$

where λ is latent heat of phase change (it is related to the temperature of the water), C is specific heat capacity of water (4.2 kJ·kg^{-1}·K^{-1}), and ΔT denotes the temperature increment of the water.

S2. Analysis of heat loss

The heat loss from the absorber consists of three losses: (1) radiation, (2) convection and (3) conduction. The details of the calculation are shown below. Consequently, the power flux consumed by solar-driven evaporation, P_{evap}, can be described as:

$$P_{evap} = P_{light} - P_{environment} = \alpha A q_{solar} - A\varepsilon\sigma\left(T^4 - T_\infty^4\right) - A q_{wter} \quad \text{(S3)}$$

The solar-vapor evaporation efficiency, η_{evap}, can be described as:

$$\eta_{evap} = \alpha - \eta_{rad,N} - \eta_{conv,N} - \eta_{cond,N} \quad \text{(S4)}$$

S2.1. Radiation loss $\eta_{rad,N}$

It is assumed that the absorber has a maximum emissivity of 0.99. For radiation loss to an ambient temperature of 26°C under 1 kW·m^{-2}, the radiation loss was calculated by the Stefan–Boltzmann:

$$E_R = \varepsilon \cdot A\sigma\left(T^4 - T_\infty^4\right) \quad \text{(S5)}$$

wherein E_R denotes heat flux, ε is the emissivity, A is the surface area (3.8 cm^2), σ is the Stefan–Boltzmann constant (5.67 × 10^{-8} W·m^{-2}·K^{-4}), T is the temperature of the absorber (35°C), and T_∞ is the ambient temperature in the experiment (31°C). Due to the top surface of the absorber being surrounded by water and heated vapor, the temperature of the adjacent environment on top of the absorber is close to the temperature of the absorber and the vapor [S1]. A thermocouple was placed near the top of the absorber surface in this work, and the measured temperature is approximately 31°C. Therefore, based on Eq. (S1), the radiation heat loss of the device was calculated to account for ~0.96% of all irradiation energy.

S2.2. Convection loss $\eta_{conv,N}$

The convection loss was calculated according to Newton's law of cooling:

$$Q = Ah\left(T - T_\infty\right) \quad \text{(S6)}$$

wherein Q denotes the heat, h is the convection heat transfer coefficient, and A is the surface area (3.8 cm^2). The convection heat transfer coefficient is approximately 5 W·m^{-2}·K^{-1}. Therefore, based on Eq. (S2), the convection heat loss of the device was calculated to account for ~5.93% of all irradiation energy.

S2.3. Conduction loss $\eta_{cond,N}$

The conduction loss was calculated based on the Eq. (7):

$$Q = Cm \cdot \Delta T \quad \text{(S7)}$$

wherein Q denotes the heat, C is the specific heat capacity of water (4.2 J·g^{-1}·°C^{-1}), m is the water weight (1.5 g), and ΔT (0.5°C) is the resulting delta in water temperature within that arises within t seconds (3,600 s). Therefore, based on Eq. (S3), the conduction heat loss of the device was calculated to account for ~2.43% of all irradiation energy.

Based on the breakdown of the three sources of heat loss, the theoretical efficiency of solar-vapor evaporation is calculated to be ~82.38% ($\eta_{evap} = \alpha - \eta_{rad,N} - \eta_{conv,N} - \eta_{cond,N}$ = 91.7% – 0.96% – 5.93% – 2.43% = 82.38%), which aligns well with empirical results.

S3. Supplementary figures

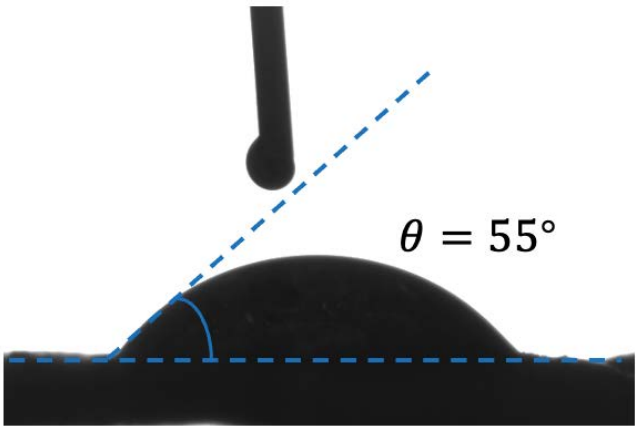

Fig. S3. Water contact angle of MXene/MD-clay/PVA film.

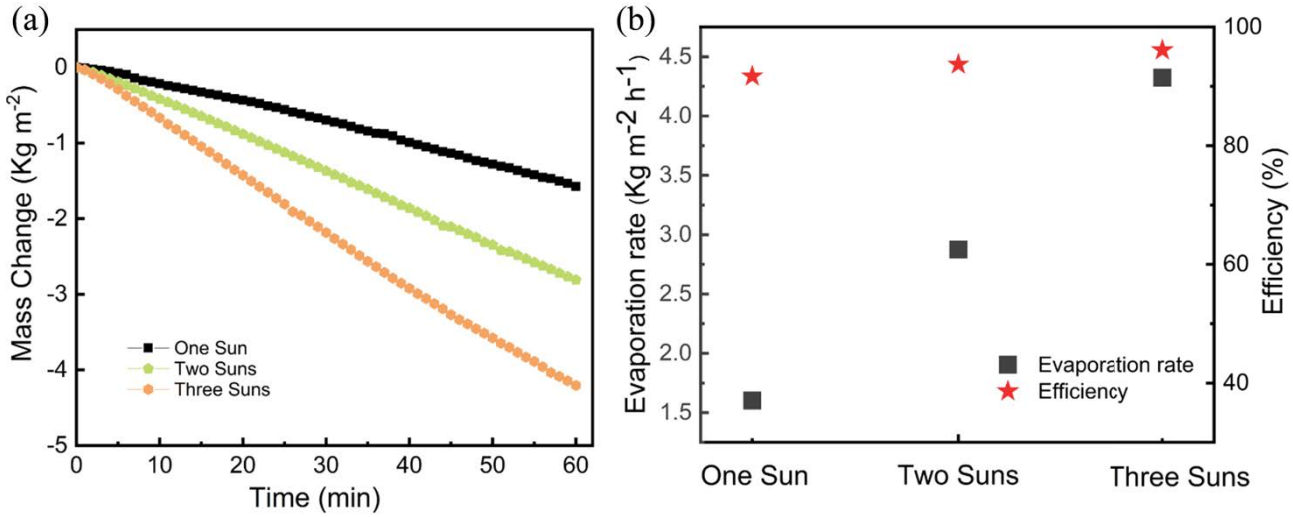

Fig. S4. (a) Water evaporation mass of MXene/MD-clay/PVA evaporator with time at 1, 2 and 3 kW·m^{-2} and (b) energy conversion efficiency and evaporation rate of MXene/MD-clay/PVA evaporator under one sun, two suns and three suns.

S4. Supplementary tables

Table S1
Photothermal conversion performance of evaporator under the irradiation of the sun with a standard optical power density of 1 kW·m^{-2}

Materials	Evaporation rate (kg·m^{-2}·h^{-1})	Photothermal conversion efficiency (%)	References
MXene-based sponge	1.41	84.8	[S2]
Three-dimensional Janus structure MXene/cellulose nanofibers/luffa aerogels	1.40	91.2	[S3]
$Ti_3C_2T_x$ MXene nanoflakes	1.43	90.14	[S4]
MXene/MnO_2 nanocomposite	1.36	85.28	[S5]
Ag-PDA@wood	1.58	88.6	[S6]
CLPM-50	1.38	–	[S7]
Janus MXene-based Photothermal membrane	1.34	90.81	[S8]
MXene/MD-clay/PVA	1.60	91.7	This work

References

[S1] S. Wu, G. Xiong, H. Yang, B. Gong, Y. Tian, C. Xu, Y. Wang, T. Fisher, J. Yan, K. Cen, T. Luo, X. Tu, Z. Bo, K. (Ken) Ostrikov, Multifunctional solar waterways: plasma-enabled self-cleaning nanoarchitectures for energy-efficient desalination, Adv. Energy Mater., 9 (2019) 1–11.
[S2] Q. Zhang, Z. Fu, H. Yu, S. Chen, Nanoplating of a SnO_2 thin-film on MXene-based sponge for stable and efficient solar energy conversion, J. Mater. Chem. A, 8 (2020) 8065–8074.
[S3] P.-L. Wang, W. Zhang, Q. Yuan, T. Mai, M.-Y. Qi, M.-G. Ma, 3D Janus structure MXene/cellulose nanofibers/luffa aerogels with superb mechanical strength and high-efficiency desalination for solar-driven interfacial evaporation, J. Colloid Interface Sci., 645 (2023) 306–318.
[S4] Y. Wang, J. Nie, Z. He, Y. Zhi, X. Ma, P. Zhong, $Ti_3C_2T_x$ MXene nanoflakes embedded with copper indium selenide nanoparticles for desalination and water purification through high-efficiency solar-driven membrane evaporation, ACS Appl. Mater. Interfaces, 14 (2022) 5876–5886.
[S5] A.M. Saleque, S. Ma, A.K. Thakur, R. Saidur, T.K. Han, M.I. Hossain, W. Qarony, Y. Ma, R. Sathyamurthy, Y.H. Tsang, MXene/MnO_2 nanocomposite coated superior salt-rejecting biodegradable luffa sponge for efficient solar steam generation, Desalination, 554 (2023) 116488, doi: 10.1016/j.desal.2023.116488.
[S6] J. Yang, Y. Chen, X. Jia, Y. Li, S. Wang, H. Song, Wood-based solar interface evaporation device with self-desalting and high antibacterial activity for efficient solar steam generation, ACS Appl. Mater. Interfaces, 12 (2020) 47029–47037.
[S7] Y. Wu, X. Zhong, Y. Li, H. Li, Y. Cai, W. Wang, X. Min, J. Xiong, M. Li, Fully waste-based solar evaporator in interfacial solar-driven seawater desalination, J. Environ. Chem. Eng., 11 (2023) 110879, doi: 10.1016/j.jece.2023.110879.
[S8] J. Su, Y. Xie, P. Zhang, R. Yang, B. Wang, H. Zhao, Y. Xu, X. Lin, J. Shi, C. Wang, Janus MXene-based photothermal membrane for efficient and durable water evaporation, Desalination, 566 (2023) 116905, doi: 10.1016/j.desal.2023.116905.